Interaction and Multiscale Mechanics, Vol. 2, No. 2 (2009) 109-128

DOI: http://dx.doi.org/10.12989/imm.2009.2.2.109

Computational multiscale analysis in civil engineering

H.A. Mang[1†], E. Aigner[1], J. Eberhardsteiner[1], C. Hackspiel[1], C. Hellmich[1], K. Hofstetter[1], R. Lackner[2], B. Pichler[1], S. Scheiner[1], R. Stürzenbecher[1]

[1]Institute for Mechanics of Materials and Structures, Vienna University of Technology, Karlsplatz 13, 1040 Vienna, Austria
[2]Material-Technology Unit, Institute for Construction and Materials Science, University of Innsbruck, Technikerstrasse 13, 6020 Innsbruck, Austria

(Received December 31, 2008, Accepted February 8, 2009)

Abstract. Multiscale analysis is a stepwise procedure to obtain macro-scale material laws, directly amenable to structural analysis, based on information from finer scales. An essential ingredient of this mode of analysis is mathematical homogenization of heterogeneous materials at these scales. The purpose of this paper is to demonstrate the potential of multiscale analysis in civil engineering. The materials considered in this work are wood, shotcrete, and asphalt.

Keywords: multiscale engineering; New Austrian Tunneling Method; wood; asphalt

1. Introduction

Recently, Fish (2008) pondered over the “hype and reality” of multiscale computations. Being a relatively new field, “it begins with naive euphoria …”. Almost always there is an “overreaction to ideas that are not fully developed, and this inevitably leads to a crash …”. “Many new technologies evolve to this point, and then fade away. The ones that survive do so because industry finds a “good use”.

In a traditional field such as civil engineering the readiness for a departure from traditional modes of design and analysis strongly depends on the probability of economic gains resulting from the use of new technologies. The expectation of such gains has motivated parts of the Austrian construction industry to support scientific research at the Institute for Mechanics of Materials and Structures of Vienna University of Technology in the area of multiscale engineering.

The following three topics in this area, with an emphasis on computational analysis in civil engineering, will be covered in this paper:

1. development and experimental verification of a continuum micromechanics model for the elasticity of wood,
2. safety assessment of shotcrete shells within the framework of the New Austrian Tunneling Method (NATM),

† Professor, Corresponding author, E-mail: Herbert.Mang@tuwien.ac.at

3. multiscale modelling of creep of asphalt - performance-based optimization of flexible pavements.

2. Development and experimental verification of a continuum micromechanics model for the elasticity of wood

Wood and many other biological materials are characterized by an astonishing variability and diversity. Their hierarchical organizations are often well suited and seemingly optimized to fulfill specific mechanical functions. This has motivated research in the fields of bionics and biomimetics. The aforementioned optimization is primarily driven by selection during the evolution process. However, it is of great importance to notice that selection is realized at the level of the individual plant or animal and not at the material level. Therefore, material optimization in the strictest sense of the word does not take place. Rather, once a hierarchical composite material has been adopted within a living organism, its fundamental building principles (morphologies or universal patterns of architectural organization (Gould and Lewontin 1979)) remain largely unchanged during evolution. Hence, entire classes of biological materials exhibit common universal principles of (micro) mechanical design (Fritsch and Hellmich 2007). In quantitative terms, such building principles can be suitably formulated in the framework of continuum micromechanics.

In continuum micromechanics (Zaoui 2002), a material is understood as a microheterogeneous body filling a representative volume element (RVE) of characteristic length l, $l \gg d$, d standing for the characteristic length of inhomogeneities within the RVE. The "homogenized" mechanical behavior of the material, i.e., the relation between homogeneous deformations acting on the boundary of the RVE and resulting (average) stresses, can then be estimated from the mechanical behavior of different homogeneous phases, representing the inhomogeneities within the RVE, their dosages within the RVE, characteristic shapes, and interactions. Based on matrix-inclusion problems (Eshelby 1957, Laws 1977), an estimate of the "homogenized" stiffness of a material reads as (Zaoui 2002)

$$\mathrm{C}^{\mathrm{hom}} = \sum_i f_i \cdot \mathrm{C}_i : [\mathrm{I} + \mathrm{P}_i^0 : (\mathrm{C}_i - \mathrm{C}^0)]^{-1} : \left\{ \sum_j f_j \cdot [\mathrm{I} + \mathrm{P}_j^0 : (\mathrm{C}_j - \mathrm{C}^0)]^{-1} \right\}^{-1} \tag{1}$$

where C_i and f_i denote the elastic stiffness and the volume fraction of phase i, respectively, and I is the fourth-order unity tensor. The two sums are taken over all phases of the heterogeneous material in the RVE. The fourth-order tensor P_i^0 accounts for the characteristic shape of phase i in a matrix with stiffness C^0. The choice of this stiffness describes the interactions between the phases. For C^0 coinciding with one of the phase stiffnesses (Mori-Tanaka scheme), a composite material is represented (contiguous matrix with inclusions); for $\mathrm{C}^0 = \mathrm{C}^{\mathrm{hom}}$ (self-consistent scheme), a dispersed arrangement of the phases is considered which is typical for polycrystals.

If a single phase itself exhibits a heterogeneous microstructure, its mechanical behavior can be estimated by introduction of RVEs within this phase, with dimensions $l_2 \ll d$, comprising again smaller phases with characteristic length $d_2 \ll l_2$, and so on, leading to a multistep homogenization scheme (Fig. 1).

Such a multistep homogenization scheme, developed by Hofstetter *et al.* (2005), suitably represents the intrinsic structural hierarchy of wood across all different tree species (Fengel and Wegener 2003). The nanoscaled components of the wood cell wall, namely crystalline cellulose,

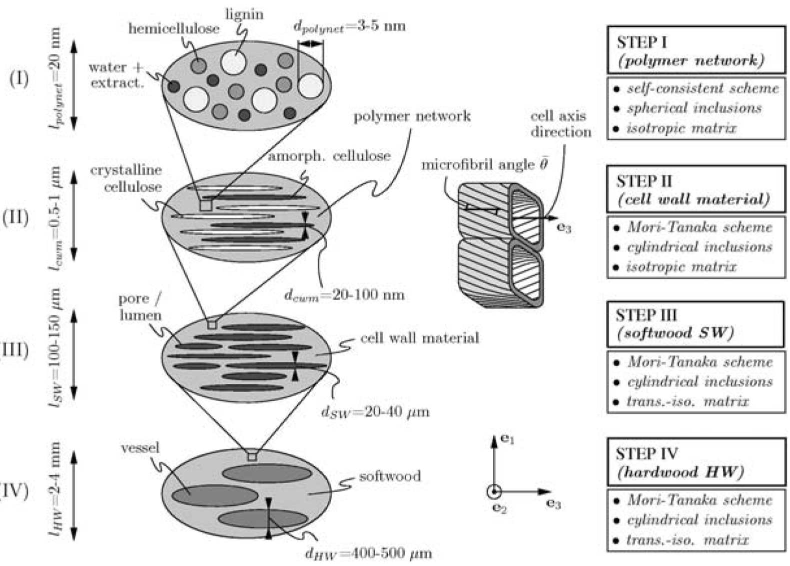

Fig. 1 Four-step homogenization scheme for wood

amorphous cellulose, hemicellulose, lignin, and water, exhibit universal elastic properties inherent to all wood species. They allow for prediction of wood tissue-specific macroscopic elastic properties from tissue-specific chemical composition and microporosity by means of the four-step homogenization scheme of Fig. 1 (Hofstetter *et al*. 2005): the first two steps are concerned with the mixture of hemicellulose, lignin, and water, lumped together with extractives, at a length scale of some nanometers in an amorphous material denoted as *polymer network*, and the embedding of inclined fiber-like aggregates of crystalline cellulose and amorphous cellulose, exhibiting typical diameters of 20-100 nm, in this polymer network, constituting the *cell wall material*. The "homogenized" stiffnesses of the polymer network and of the cell wall material are determined by means of continuum micromechanics, namely though self-consistent and Mori-Tanaka homogenization steps, respectively, as described in (Hofstetter *et al*. 2005). At a length scale of about one hundred microns, the material *softwood* is defined, comprising cylindrical pores (lumens) in the cell wall material of the preceding homogenization step. Its stiffness can again be estimated by means of the Mori-Tanaka scheme. Finally, at a length scale of several millimeters, *hardwood* comprises additional larger cylindrical pores denoted as vessels which are embedded in the softwood-type material homogenized before. Estimates of the stiffness of hardwood are derived in an analogous manner in the third homogenization step.

The approximately periodic arrangement of the wood cells renders the Unit Cell Method also highly suitable for the third homogenization step. In this method, the real material microstructure is represented by a periodic arrangement of identical basic repetitive units which are considered in a discrete manner. Since the length of the wood cells, l_L, is about 100 times larger than their cross-sectional dimensions, the assumption of an infinite extension of the unit cell in the direction of the longitudinal axis L is justified. The hexagonal shape of the unit cell is specified in terms of the ratio of the mean tangential lumen diameter, l_T, to the mean radial lumen diameter, l_R, (cross-sectional aspect ratio $\lambda = l_T / l_R$), and of the inclination angle of the radial cell walls, α (Fig. 2).

The unit cell is subjected to periodic, symmetric or antisymmetric boundary conditions for the

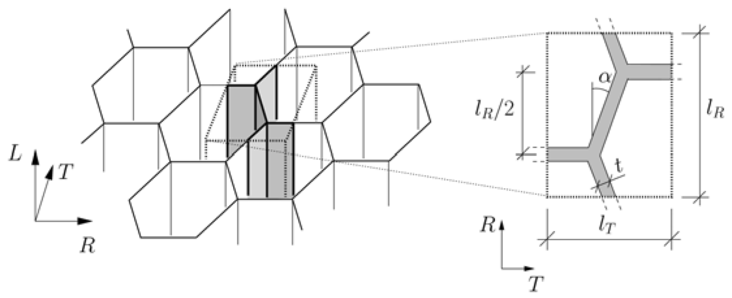

Fig. 2 Unit cell for softwood material

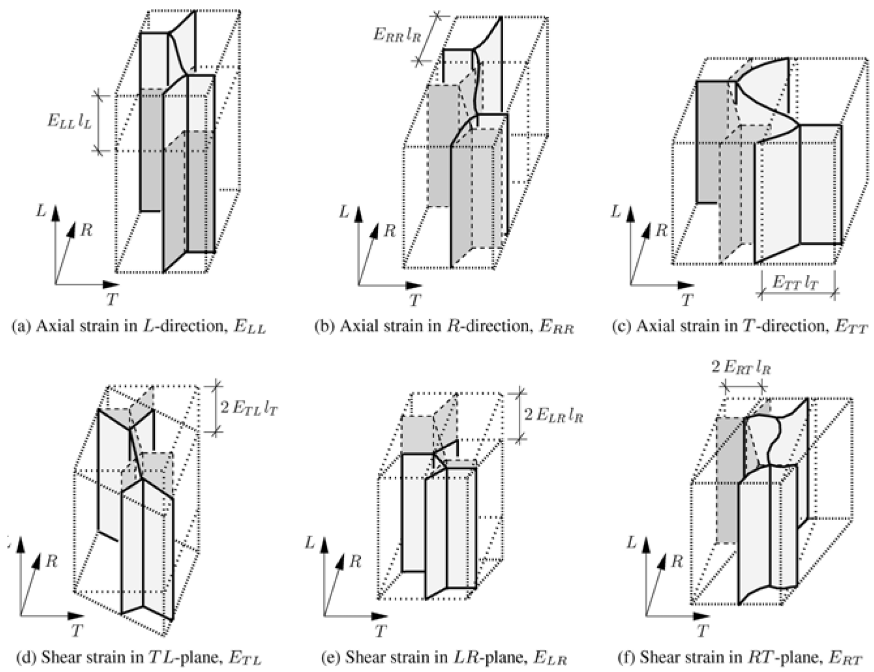

Fig. 3 Displacement configurations of unit cell related to six reference strain states E_{ij}, $i, j = L, R, T$

displacements, such that the spatial averages of the corresponding strains are equal to the macroscopic strains related to the cellular material. Linking these macroscopic strains to the spatial average of the periodic microstresses they create, i.e., to the macroscopic stresses, yields the homogenized effective stiffness of the cellular material. In detail, six independent displacement configurations are imposed to the boundary of the unit cell so as to create unit values of macroscopic strain components, E_{ij}, $i, j = L, R, T$:

- a unit axial strain in the longitudinal direction L is created by symmetric displacements, $E_{LL}l_L$, at the boundary [Fig. 3(a)],
- a unit axial strain in the radial direction R is created by periodic radial displacements, $E_{RR}l_R$, at the boundary [Fig. 3(b)],
- a unit axial strain in the tangential direction T is created by symmetric tangential displacements,

$E_{TT}l_T$, at the boundary [Fig. 3(c)],

- a unit shear strain in the *LT*-plane and the *LR*-plane is created by antisymmetric longitudinal displacements, $2E_{TL}l_T$ and $2E_{LR}l_R$, respectively, [Figs. 3(d,e)], and
- a unit shear strain in the *RT*-plane is created by antisymmetric tangential displacements, $2E_{RT}l_R$ [Fig. 3(f)].

The spatial averages of the corresponding periodic (normal and shear) microstresses are equal to the components of the homogenized stiffness tensor of softwood (Hofstetter *et al.* 2007).

The capability of this method to capture plate-like bending and shear deformations of the cell walls at transverse loading results in better estimates of the transverse shear modulus and of the tangential elastic modulus (Hofstetter *et al.* 2007).

Validation of the presented continuum micromechanics model rests on statistically and physically independent experiments: the macroscopic material stiffness predicted by the micromechanical model on the basis of tissue-independent ("universal") phase stiffness properties of hemicellulose, amorphous cellulose, crystalline cellulose, lignin, and water (*experimental set Ia*) and of tissue-independent mean values of the morphological characteristics (*experimental set Ib*) for tissue-specific composition data (*experimental set IIb*) are compared to corresponding experimentally determined tissue-specific stiffness values (*experimental set IIa*) (Hofstetter *et al.* 2005). For the elastic moduli in the longitudinal direction (aligned with the stem axis), E_L, and in the transverse direction (in the cross-sectional plane of the stem), E_T, as well as for the shear modulus in the plane through the longitudinal axis, G_L, model estimates and experimental results show good agreement over a large variety of wood species (Fig. 4).

Micromechanical models for wood are expected to support optimization processes in wood drying technology and structural analyses of wood structures (Mackenzie-Helnwein *et al.* 2005), such as, e.g., the elastoplastic numerical simulation of a barrel shell with a central opening (Fig. 5a) or of a typical timber joint, a break joint (Fig. 5b). Validation of such analyses is preferably done by structural testing as shown in Fig. 5c for a glulam bending beam with a circular hole (Fleischmann *et al.* 2007).

Continuum micromechanics also constitutes a powerful tool for the mechanical characterization of wood products such as the innovative Veneer Strand Board (VSB). It consists of large-area, flat and slender strands with uniform strand shape and dimensions (see Fig. 6) and is typically built up of several layers with different strand orientations. The high-quality strand material results in increased stiffness and strength of the board compared to conventional strand and Veneer-based panels. The latter are typically used for sheeting and stiffening purposes, whereas the improved mechanical behavior of the VSB allows for an extension of the range of possible applications to the load-

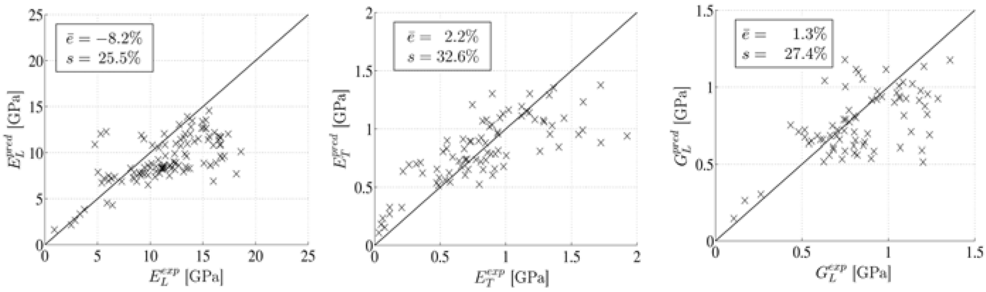

Fig. 4 Comparison of predicted and measured elastic constants

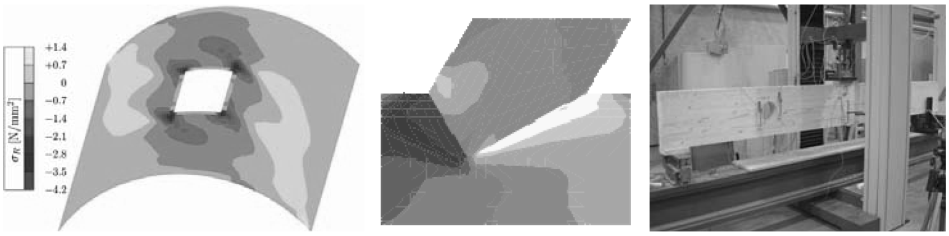

Fig. 5 Experimental investigation and FE analyses of wooden structures (a) distribution of stress component perpendicular to the fiber direction, (b) distribution of inplane component of shear stresses, and (c) experimental set-up of structural test (Mackenzie-Helnwein *et al*. 2005, Fleischmann *et al*. 2007)

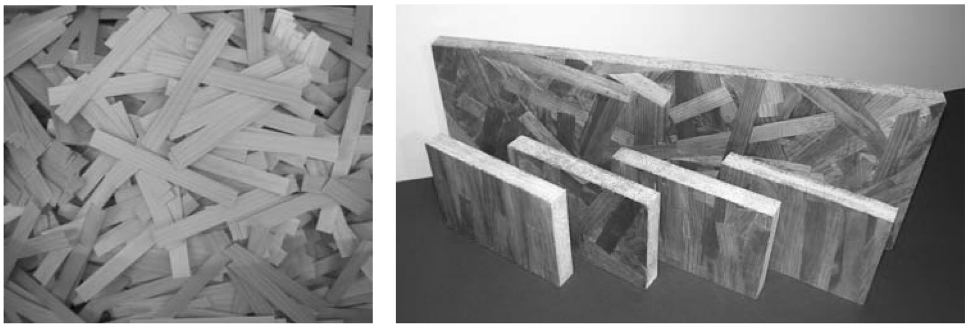

Fig. 6 Veneer strands and finished board

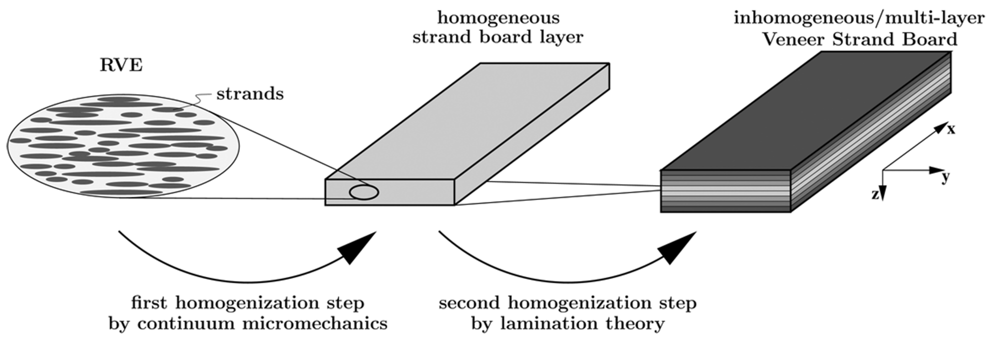

Fig. 7 Hierarchical levels of strand boards and respective homogenization procedures

bearing sector. The development of a multiscale model for the analysis of the mechanical behavior of such boards has enabled identification of optimal strand dimensions and orientations as well as promising vertical build-ups in terms of the density profile and the layer structure.

The multiscale model spans three scales of observations: the strand material, a homogeneous board layer, and the multi-layer board (Fig. 7).

At first, continuum micromechanics is applied to estimate the elastic properties of a homogeneous board layer from the stiffness of the strands, their shape, and their orientation. The strands are connected by a synthetic adhesive which does not act as an own material phase but contributes to the mechanical behavior of the compound by two substantial effects: first, the adhesive penetrates the wood tissue of the strands and compensates micro-damages in consequence of the strand production. Second, it establishes the crucial bonding between the strands, which is assumed to be perfect in the model. The absence of a contiguous matrix phase in the board motivates the use of the implicit self-consistent scheme. The strands constitute the only phase of the model, which is made up of inclusions with different orientations. The orientation distribution of the strands in the plane of the panel is described in terms of a distribution function $g_s(\varphi)$, where the angle φ denotes the inclination of the principal axis of the strand to the main axis of the strand board. Considering the morphologically and mechanically justified periodicity of π, specification of Eq. (1) for the strand board layer reads as

$$\mathrm{C}^{\mathrm{hom}} = \left\{ \int_{\varphi=-\frac{\pi}{2}}^{+\frac{\pi}{2}} \mathrm{C}_s(\varphi):[\mathrm{I} + \mathrm{P}_s^{\mathrm{hom}}(\varphi):(\mathrm{C}_s(\varphi) - \mathrm{C}^{\mathrm{hom}})]^{-1} g_s(\varphi) d\varphi \right\}: \left\{ \int_{\varphi=-\frac{\pi}{2}}^{+\frac{\pi}{2}} [\mathrm{I} + \mathrm{P}_s^{\mathrm{hom}}(\varphi):(\mathrm{C}_s(\varphi) - \mathrm{C}^{\mathrm{hom}})]^{-1} g_s(\varphi) d\varphi \right\}^{-1} \quad (3)$$

where $g_s(\varphi)$ meets the normality condition

$$\int_{\varphi=-\frac{\pi}{2}}^{+\frac{\pi}{2}} g_s(\varphi) d\varphi = 1 \quad (4)$$

C_s denotes the stiffness tensor of the compacted, adhesive-penetrated strands. The fourth-order tensor $\mathrm{P}_s^{\mathrm{hom}}$ is obtained by treating the strands as infinitely long cylinders with elliptic cross-sections (Laws 1977 and Mura 1987) , with an aspect ratio of 25; the longer extension is parallel to the panel plane.

In the second step, effective stiffness properties of a multi-layer panel are determined by means of classical lamination theory. Thereby, the stacking sequence, the orientation of the principal material directions of the single layers, and the density variation across the board thickness are taken into account (Stürzenbecher *et al.* 2008).

Model validation is again based on independent experiments. For this purpose, homogeneous boards as well as inhomogeneous boards with a well defined vertical density distribution were produced. As for the homogeneous boards, three different distributions of the strand orientation [random (R), aligned (O), and crosswise (X)], three different wood qualities [good (G), medium, and poor (P)], and two different density levels [high and low (LD)] were considered. The inhomogeneous boards varied mainly by the stacking sequence, including single-layer boards with constant strand-orientation distribution across the board thickness and also three-layer boards with alternating strand orientations in subsequent layers.

The mechanical testing of strands, homogeneous boards, and inhomogeneous/multi-layer boards allows for independent validation of both modeling steps based on continuum micromechanics and on lamination theory, respectively. Altogether, good agreement of experimental data and corresponding model predictions was observed. Correlation plots of experimental and numerical results for the two in-plane elastic moduli E_x and E_y as well as for the two shear moduli G_{yz} and G_{xz} of homogeneous boards are shown in Fig. 8. Corresponding plots for inhomogeneous/multi-layer boards can be found in Stürzenbecher *et al.* (2008). The good agreement underlines the capability of the model for stiffness estimation of strand-based engineered wood products by means of microstructural features and renders it a powerful tool for parameter studies and product optimization.

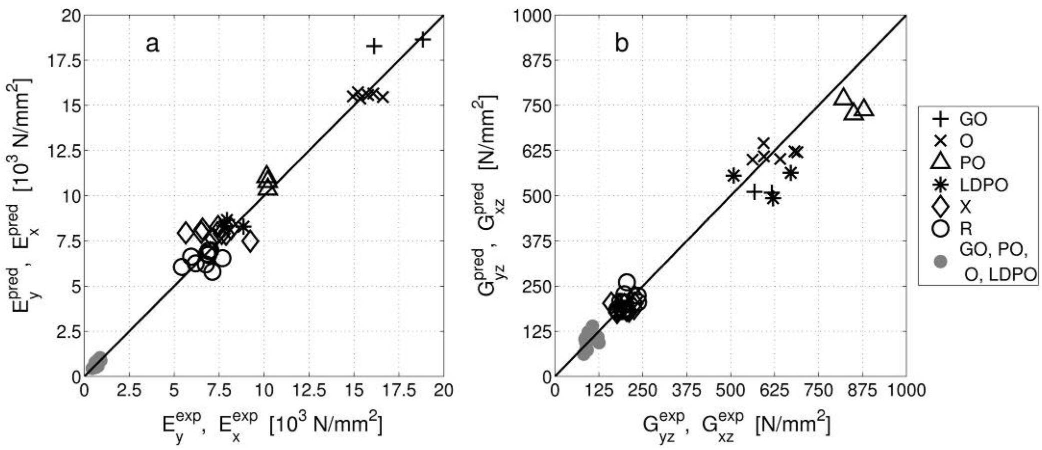

Fig. 8 Comparison of experimental data and corresponding model predictions for the in-plane moduli of elasticity E_y and E_x and the shear moduli G_{yz} and G_{xz} of homogeneous strand boards

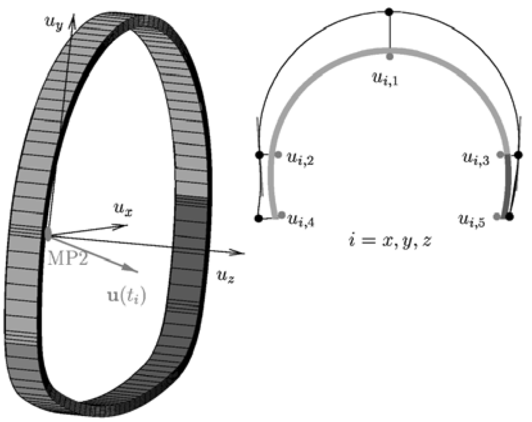

Fig. 9 Hybrid method (Hellmich *et al.* 2001) for determination of the level of loading from prescription of measured displacements as boundary values for a three-dimensional Finite Element model of the tunnel shell

3. Safety assessment of shotcrete shells within the framework of the New Austrian Tunneling Method (NATM)

In the New Austrian Tunneling Method (NATM), a shotcrete shell is used as primary support for the freshly excavated stretch of the tunnel. Elaborate monitoring devices allow for estimation of the forces in the tunnel shell, e.g. through a hybrid method (Hellmich *et al.* 2001), in which displacement vector fields are approximated from measured displacement vectors at discrete points of the tunnel shell and in which these fields are prescribed as boundary values for a three-dimensional Finite Element structural model of the tunnel shell (see Fig. 9).

The structural computation requires an elaborate material model for shotcrete, accounting for mechanical properties that change because of hydration. Recent advances in micromechanics and nanotechnology have opened a new gateway to relationships between the hydration degree and the

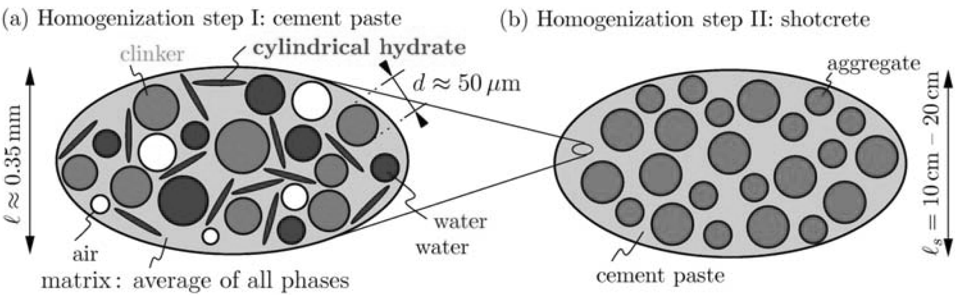

Fig. 10 Two-scale homogenization model for shotcrete

mechanical properties: based on mathematical descriptions of the material morphology within representative volume elements, shotcrete-independent constituents (cement clinker, hydrates, water, air, aggregates) and their hydration degree-dependent dosages define the overall material behavior. Emphasis is laid on two key material properties of shotcrete, elasticity (Hellmich and Mang 2005) and strength (Pichler *et al.* 2008). Therefore, we consider two representative volume elements (Pichler *et al.* 2008) (see Fig. 10).

At the level of the cement paste, four material phases are considered: clinker, hydration products, water, and air. A spherical geometry is assigned to clinker grains and pores, and acicular (needle-type) shapes to the micrometer-sized hydration products, which are uniformly distributed in all directions of space (Pichler *et al.* 2009).

The elastic properties of the cement paste are upscaled (homogenized) from the intrinsic ("universal") elastic properties of its constituents, in the framework of continuum micromechanics. In detail, the upscaled stiffness tensor of cement paste, $\mathbf{C}_{cp}$, reads as (Pichler *et al.* 2009)

$$\mathbf{C}_{cp} = \left\{ \sum_p f_p \mathbf{c}_p : [\mathbf{I} + \mathbf{P}^{cp}_{sph} : (\mathbf{c}_p - \mathbf{C}_{cp})]^{-1} + f_{hyd}\, \mathbf{c}_{hyd} : \int_{\varphi=0}^{2\pi} \int_{\vartheta=0}^{\pi} [\mathbf{I} + \mathbf{P}^{cp}_{cyl}(\varphi, \vartheta) : (\mathbf{c}_{hyd} - \mathbf{C}_{cp})]^{-1} \frac{\sin\vartheta}{4\pi} d\vartheta d\varphi \right\} :$$
$$\left\{ \sum_p f_p [\mathbf{I} + \mathbf{P}^{cp}_{sph} : (\mathbf{c}_p - \mathbf{C}_{cp})]^{-1} + f_{hyd} \int_{\varphi=0}^{2\pi} \int_{\vartheta=0}^{\pi} [\mathbf{I} + \mathbf{P}^{cp}_{sph}(\varphi, \vartheta) : (\mathbf{c}_{hyd} - \mathbf{C}_{cp})]^{-1} \frac{\sin\vartheta}{4\pi} d\vartheta d\varphi \right\}^{-1} \tag{5}$$

with f_p and $\mathbf{c}_p$ as the volume fractions and stiffness tensors of material phases p, $p =$ clinker, H_2O, air, f_{hyd} and $\mathbf{c}_{hyd}$ as the volume fraction and the stiffness tensor, respectively, of the hydrate phase, $\mathbf{I}$ as the fourth-order unit tensor, $\mathbf{P}^{cp}_{sph}$ as the Hill tensor of a spherical phase embedded in a matrix with stiffness $\mathbf{C}_{cp}$, $\mathbf{P}^{cp}_{sph}(\varphi, \vartheta)$ as the Hill tensor of the acicular-shaped hydrate phase embedded in a matrix with stiffness tensor $\mathbf{C}_{cp}$, and φ and ϑ as the Euler angles defining the orientations of the hydrate needles, see (Pichler *et al.* 2009) for details. For detailed explanations regarding the numerical evaluation of Eq. (5), giving access to the homogenized bulk modulus k_{cp}, the homogenized shear modulus μ_{cp}, the homogenized Young's modulus E_{cp}, and to the homogenized Poisson's ratio ν_{cp} of the cement paste, see (Pichler *et al.* 2008 and Pichler *et al.* 2009). At the shotcrete level, spherical aggregate inclusions are embedded into a contiguous matrix made up of cement paste. At this level, a Mori-Tanaka homogenization scheme is used for determination of the upscaled stiffness tensor of shotcrete, $\mathbf{C}_{sc}$, reading as (Pichler *et al.* 2008).

$$\mathbf{C}_{sc} = \{ \bar{f}_{cp}\mathbf{C}_{cp} + \bar{f}_{agg}\mathbf{c}_{agg}:[\mathbf{I} + \mathbf{P}^{cp}_{sph}:(\mathbf{c}_{agg} - \mathbf{C}_{cp})]^{-1} \}: \{ \bar{f}_{cp}\mathbf{I} + \bar{f}_{agg}:[\mathbf{I} + \mathbf{P}^{cp}_{sph}:(\mathbf{c}_{agg} - \mathbf{C}_{cp})]^{-1} \}^{-1} \tag{6}$$

with $\bar{f}_{cp}$ and $\bar{f}_{agg}$ as the volume fractions of the cement paste and the aggregates within a representative volume element of shotcrete, $\mathbf{c}_{agg}$ as the stiffness tensor of the aggregates, and with $\mathbf{C}_{cp}$ as the stiffness tensor of the cement paste obtained from the first homogenization step (Eq. (5)).

Upscaling of strength is based on a von Mises-type elastic limit criterion for the individual hydrates. The latter are characterized by a single strength value for the hydrates, σ^{dev}_{crit} = 26 MPa (Pichler *et al.* 2009), which allows to predict early-age strength evolutions of cement pastes with *w/c*-ratios ranging from 0.35 to 0.60 (Pichler *et al.* 2009). Brittle failure-inducing deviatoric stress peaks within hydrates are estimated through quadratic stress averages which are accessible through derivation of the shotcrete elasticity with respect to the hydrate stiffness (Pichler *et al.* 2009), along the line of reasoning proposed by Dormieux *et al.* (2002). In this way, the micromechanical strength criterion is formulated in terms of macroscopic loading (stresses or strains, respectively). This criterion gives the macroscopic uniaxial compressive strength $\Sigma^{comp,ult}_{sc,11}$ as a function of hydrate strength σ^{dev}_{crit} and of the micro-characteristics of shotcrete contained in Eq. (5), reading as

$$\Sigma^{comp,ult}_{sc,11} = \left\{ \max_{\varphi,\vartheta} \left[\lim_{\Delta\varphi,\Delta\vartheta \to 0} \left(-\frac{(\mu_{hyd})^2}{\bar{f}_{hyd;\varphi,\vartheta}} (\mathbf{e}_z \otimes \mathbf{e}_z) : \frac{\partial (\mathbf{C}_{sc})^{-1}}{\partial \mu_{hyd;\varphi,\vartheta}} : (\mathbf{e}_z \otimes \mathbf{e}_z) \right)^{\frac{1}{2}} \right] \right\}^{-1} \times \sigma^{div}_{crit} \tag{7}$$

with $\bar{f}_{hyd;\varphi,\vartheta}$ denoting the volume fraction of the hydrate bundle with angular coordinates belonging to $[\varphi, \varphi + \Delta\varphi] \times [\vartheta, \vartheta + \Delta\vartheta]$, with $\mu_{hyd;\varphi,\vartheta}$ as the shear modulus of this hydrate bundle, and with $\mathbf{e}_z$ as the base vector in the *z*-direction in an orthonormal base frame, defining the loading direction in the uniaxial test. The aforementioned limit, $\lim_{\Delta\varphi,\Delta\vartheta \to 0}$, can be conveniently computed by means of a finite difference scheme, see (Pichler *et al.* 2009) for details. Good agreement between model-predicted elasticity and strength evolutions for different water-cement (*w/c*) and aggregate-cement (*a/c*) ratios underlines the predictive capability of the proposed micromechanical model, see Fig. 11.

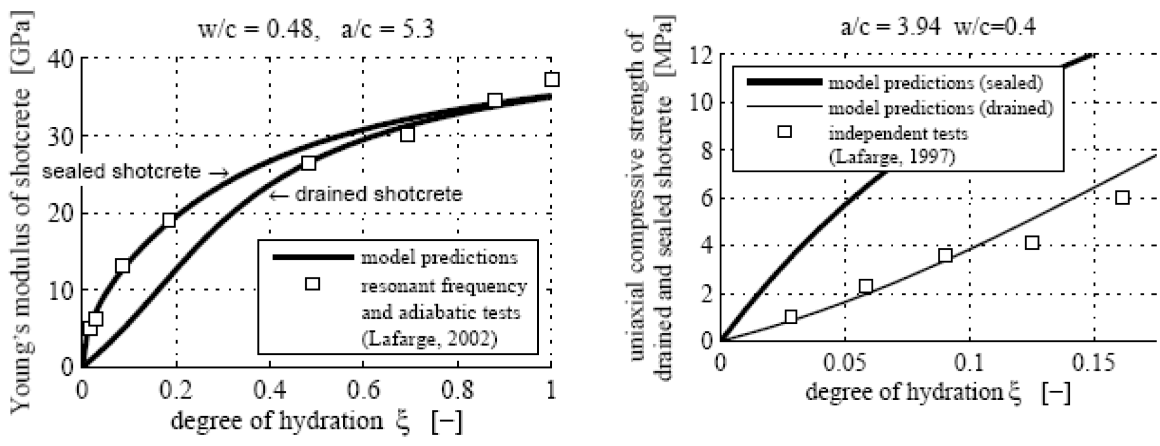

Fig. 11 Experimental validation of two-scale model for elasticity and strength of shotcrete (Pichler *et al.* 2009)

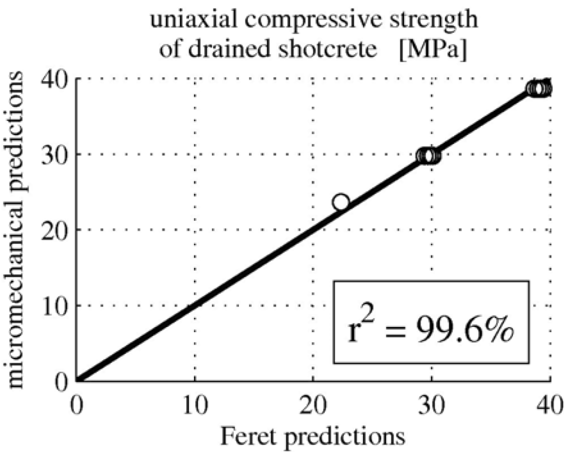

Fig. 12 Comparison of micromechanics-based model predictions with predictions by Feret's formula (Scheiner *et al.* 2008 and Feret 1892)

It is interesting to note that the predictions also perfectly match the estimates of the famous Feret formula (Feret 1892), a widely used practical tool in cement industry. Feret's empirical relationship states that the final strength, $\Sigma^{ult}(t = \infty)$, is proportional to the square of a ratio between the volumes of cement, water, and air contained in a material volume of concrete

$$\Sigma^{ult}(t = \infty) = P\left[\frac{f_{clinker}(\xi = 0)}{f_{clinker}(\xi = 0) + f_{H_2O}(\xi = 0) + f_{air}(\xi = 0)}\right]^2 \tag{8}$$

where P is a factor of proportionality. The match between this relationship (with $P = 197.2$ MPa) and the model-predicted strength at completed hydration, see Fig. 12, further corroborates the relevance of our model.

At the structural level, herein related to the Sieberg tunnel on the railway track Vienna-Salzburg (Hellmich *et al.* 2001), two types of computations are performed: (a) a thermochemical analysis for computation of hydration-induced temperature fields within the tunnel shell, and (b) a chemomechanical analysis for determination of the stress fields within the tunnel shell resulting from a given loading (in terms of prescribed displacement fields). In the course of the thermochemical analysis (Hellmich *et al.* 1999), the following governing equations are employed:

• the first law of thermodynamics,

$$C\dot{T} + L^{hyd}\dot{\xi} = -\mathrm{div}\,\mathbf{q} \tag{9}$$

relates the external heat supply $-\mathrm{div}\,\mathbf{q}$ ($\mathbf{q}$ is the heat flux vector) to the internal heat change $C\dot{T}$ (C is the heat capacity of the considered shotcrete and T is the absolute temperature), and to the latent heat production resulting from hydration $L^{hyd}\dot{\xi}$ (L^{hyd} is the heat produced at complete hydration);

• Fourier's heat conduction law,

$$\mathbf{q} = -k\,\mathrm{grad}\,T \tag{10}$$

with the heat conductivity k of shotcrete; and

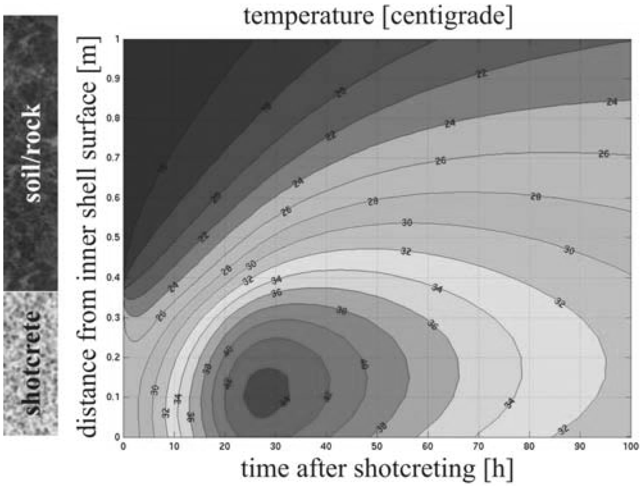

Fig. 13 Temperature evolution, in centigrade, in the tunnel shell, as a function of time [in hours] since shotcreting and of the distance [in m] from inner shell surface (shell thickness equal to 30 cm)

- a macroscopic hydration kinetics law for shotcrete, describing the evolution of the degree of hydration ξ,

$$\dot{\xi} = \tilde{A}(\xi)\exp\left(-\frac{E_a}{RT}\right) \tag{11}$$

with $\tilde{A}(\xi)$ as the normalized chemical affinity (Ulm and Coussy 1996, Hellmich *et al.* 1999), E_a as the activation energy, and R as the universal constant of ideal gas.

Based on shotcrete-specific values for C, k, L^{hyd}, E_a, and $\tilde{A}(\xi)$ (see (Hellmich and Mang 2005, Lechner *et al.* 2001, Macht *et al.* 2001) for the employed values, and for the heat characteristics of the surrounding soil), the thermochemical analysis delivers time-dependent fields of the temperature and the degree of hydration, see Fig. 13. The maximum temperature of 45 centigrades is reached around 30 hours after shotcreting at a depth of around 10 cm.

Subsequently, a chemomechanical analysis is performed, combining force equilibrium with a chemoplastic material model including creep (Sercombe *et al.* 2000)

$$\mathrm{d}\boldsymbol{\sigma} = \mathbf{C}_{sc}(\xi):[\mathrm{d}\boldsymbol{\varepsilon} - \mathrm{d}\boldsymbol{\varepsilon}^p - \mathrm{d}\boldsymbol{\varepsilon}^f - \alpha_T \mathbf{1}\mathrm{d}T - \mathbf{1}\mathrm{d}\varepsilon^s(\xi) - \mathrm{d}\boldsymbol{\varepsilon}^v] \tag{12}$$

where $\mathrm{d}\boldsymbol{\varepsilon}^p$ is an infinitesimal increment of plastic strains (at the level of a representative volume element of shotcrete), $\mathrm{d}\boldsymbol{\varepsilon}^f$ is an infinitesimal increment of long-term creep strains, $\mathrm{d}\boldsymbol{\varepsilon}^v$ is an infinitesimal increment of short-term creep strains, α_T is the coefficient of thermal dilatation, $\mathbf{1}$ is the second-order unit tensor, and $\mathrm{d}\varepsilon^s(\xi)$ is an infinitesimal increment of shrinkage strains. Simulation results are illustrated in terms of the so-called level of loading L which can be interpreted as the degree of utilization. The latter is defined as the ratio of the loading (stress) over loading capacity (strength) of the shotcrete tunnel shell. More specifically, it is defined on the basis of a Drucker-Prager failure surface calibrated for uniaxial and biaxial compressive failure, $\Sigma_{sc,11}^{comp,ult}$ from Eq. (7), and $\Sigma_{sc,11}^{Bicomp,ult} = \Sigma_{sc,11}^{comp,ult} \times \kappa$, with $\kappa = 1.16$,

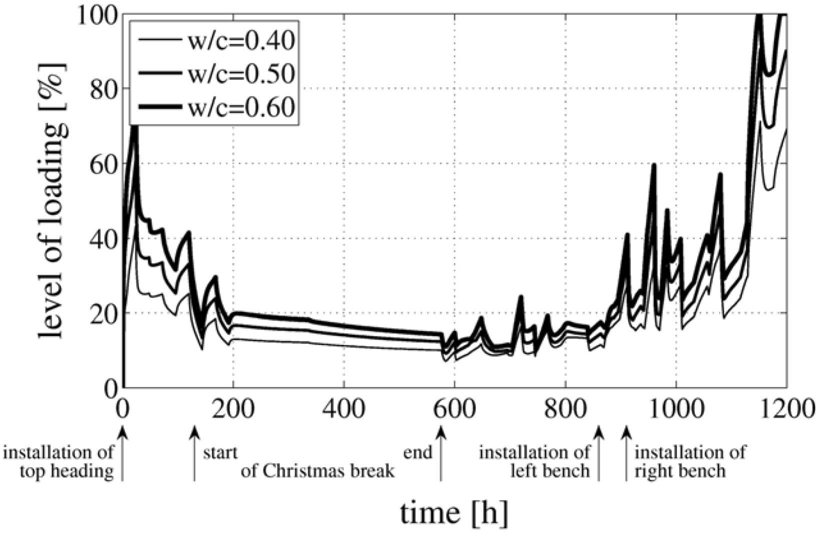

Fig. 14 Safety assessment of tunnel shell, determined on the basis of elasticity and strength values related to different *w/c* values, *a/c* = 5; the level of loading refers to a Drucker-Prager comparative stress over the current strength

$$L = \frac{\alpha \mathrm{tr}\Sigma_{sc} + \sqrt{\Sigma^{dev}_{sc,ij}\Sigma^{dev}_{sc,ij}}}{k} \text{ with } \alpha = \sqrt{\frac{2}{3}}\frac{\kappa-1}{2\kappa-1},\ k = \sqrt{\frac{2}{3}}\left(1-\frac{\kappa-1}{2\kappa-1}\right)\Sigma^{comp,ult}_{sc,11} \tag{13}$$

In the present evaluation the focus is on the average value of L over the shell thickness h,

$$\bar{L}(\varphi, t) = \frac{1}{h}\int_h L(r, \varphi, t)dr \tag{14}$$

with r and φ as polar coordinates defining (macroscopic) positions within a circular shell segment.

In Fig. 14 the maximum value of $\bar{L}(\varphi, t)$ in the tunnel shell, $\bar{L}_{\max}(t)$, is designated as the "level of loading". In Eq. (12), the elastic and strength values are used that were obtained from the proposed two-step homogenization model (with degree of hydration-dependent volume fractions according to (Pichler *et al.* 2008)), for given *w/c* values between 0.4 and 0.6, and *a/c* = 5.

The chemomechanical analyses show that throughout the observed loading phase the resulting level of loading of the tunnel shell is decisively influenced by the *w/c*-ratio, see Fig. 14. In detail, the level of loading for *w/c* = 0.40 is around 40% lower than the one of *w/c* = 0.60. At the end of the observed loading phase, 1120 hours after installation of the top heading, simulations based on *w/c* = 0.60 predict a level of loading reaching 100%. This indicates severe cracking or even failure of the tunnel shell, whereas for both *w/c* = 0.40 and *w/c* = 0.50 the tunnel shell is intact, see Fig. 14. The significant increase of the level of loading in the tunnel shell with increasing *w/c*-ratio can be explained as follows: with increasing *w/c*-ratio the percental decrease in macroscopic stiffness of shotcrete is smaller than the percental decrease in the uniaxial compressive strength of the material (for a detailed presentation of corresponding micromechanics-based material functions, see (Pichler *et al.* 2008)). Whereas a slightly reduced elastic stiffness activates only slightly smaller forces within the shotcrete tunnel shell, a more pronounced loss in uniaxial compressive strength significantly reduces the load-carrying capacity of the material. Hence, the larger the water-cement

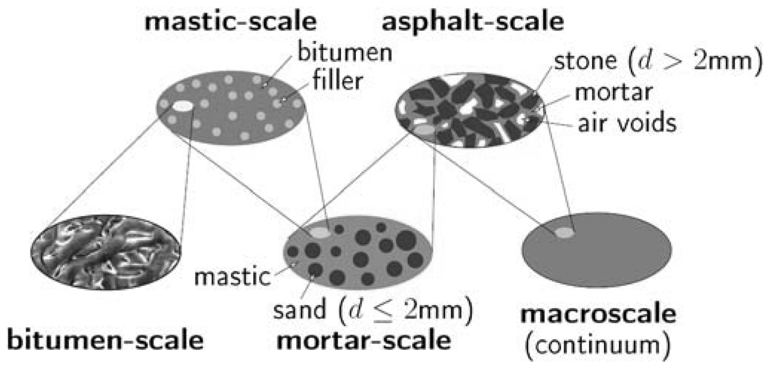

Fig. 15 Multiscale model used for asphalt

ratio, the smaller the material resistance. The reduced load-carrying capacity cannot be compensated by smaller forces in the tunnel shell caused by the reduced stiffness of the material. It is concluded that rather small *w/c*- ratios (that is, high cement contents) are beneficial to shotcrete tunnel shells. This further motivates the development of additives which reduce water contents typically encountered in real-life applications.

4. Upscaling of Viscoelastic Properties of Matrix-inclusion Materials in the Framework of Multiscale Modeling - Application to Asphalt

The rapid degradation of the road infrastructure was the reason for founding the Christian-Doppler Laboratory for "Performance-based optimization of flexible pavements" at Vienna University of Technology. Currently, a multiscale model for asphalt is being developed in this laboratory (Lackner *et al.* 2004), allowing identification of fundamental mechanisms of behavior of asphalt at several observation scales. By means of application of advanced upscaling methods, the gain in knowledge at the finer scales is translated to the structural scale and finally used for the design of new pavement structures and the assessment of existing ones. To utilize the benefits of multiscale characterization and modeling of materials, such as (i) incorporation of physical/chemical processes at the scale of their occurrence and (ii) goal-oriented optimization of materials, requires great efforts as regards both experimental and theoretical research. In fact, recent progress in theoretical micromechanics and the experimental identification of material properties at finer scales paved the way for validated bottom-up multiscale models for bio- and building materials. Here, recent developments in upscaling of viscoelastic properties are presented and applied to asphalt, characterized by aggregates of different size embedded into a bitumen matrix (see Fig. 15).

Viscoelasticity is used to describe the behavior of materials showing an accumulation of strains under constant stress (creep) and/or a reduction of stress under constant strain (relaxation). Depending on the prescribed quantity (strain or stress), the respective unknown quantity (stress or strain) is determined, using the relaxation modulus $E(t) = \sigma(t) / \varepsilon_0$ and the creep compliance $J(t) = \varepsilon(t) / \sigma_0$, respectively. E.g., for a specified stress history $\sigma(t)$, the strain at the time instant t reads,

$$\varepsilon(t) = \int_0^t J(t-\tau)\frac{\partial\sigma(\tau)}{\partial\tau}d\tau \tag{15}$$

with a Laplace-Carson[1] transformation reading

$$\varepsilon^*(p) = J^*(p)\sigma^*(p) \tag{16}$$

The analogy between Eq. (16) and the linear-elastic constitutive law $\sigma = E\varepsilon$ is the basis for the solution of viscoelastic problems within the correspondence principle. Hereby, the material parameters in the solution of the respective elastic problem are replaced by the respective Laplace-Carson transformed viscoelastic parameters (Aigner and Lacker 2008, Aigner *et al.* 2007). E.g., the elastic shear compliance $1/\mu$ is replaced by the Laplace-Carson transformed creep-compliance function for deviatoric creep, $J_{dev}{}^*(p)$. The inverse Laplace-Carson transformation delivers the corresponding solution in the time space.

Upscaling of rheological properties of bitumen-aggregate composites is performed in the framework of continuum micromechanics, formulating the Mori-Tanaka scheme in the Laplace-Carson space. The elastic-viscoelastic correspondence principle gives access to the effective (homogenized) creep compliance of a matrix/inclusion-composite as

$$J^*_{eff}(p) = \frac{f_M + f_I[1 + \beta^*(J^*_M/J^*_I - 1)]^{-1}}{f_M/J^*_M + f_I/J^*_I[1 + \beta^*(J^*_M/J^*_I - 1)]^{-1}} \tag{17}$$

with $\beta^* = 6(k^*_M + 2J^*_M)/[5(3k^*_M + 4J^*_M)]$. For the case of deviatoric creep of the matrix and elastic behavior of the inclusions, $k^*_M = k_M$ and $1/J^*_I = \mu_I$. Finally, the inverse Laplace-Carson transformation delivers the effective creep compliance of the composite material in the time domain:

$$J_{eff}(t) = \mathrm{LC}^{-1}[J^*_{eff}(p)] \tag{18}$$

Whereas the inversion can be performed analytically for simple rheological models, numerical inversion (employing, e.g., the Gaver-Stehfest algorithm (Stehfest 1970)) is needed for material phases showing a complex rheological behavior. Hereby, the transformation provides discrete points of the effective creep compliance function $J_{eff}(t)$. Approximation of $J_{eff}(t_i)$ by a creep-compliance function affine to the rheological behavior of the material phases exhibiting time-dependent behavior gives access to the effective viscoelastic model parameters.

---

[1] The Laplace-Carson transformation of $f(t)$ is given as

$$\mathrm{LC}[f(t)] = f^*(p) = p\int_0^\infty f(t)e^{-pt}dt$$

The inverse Laplace-Carson transformation is defined in the complex plane as

$$\mathrm{LC}^{-1}[f^*(p)] = f(t) = \frac{1}{2i\pi}\int_\Omega \frac{f^*(p)}{p}e^{pt}dp$$

where Ω is a parallel to the imaginary axis having all poles of $f^*(p)$ to the left.

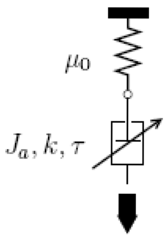

$$J(t) = \frac{1}{\mu_0} + J_a\left(\frac{t}{\tau}\right)^k$$
$$J^*(p) = \mathcal{LC}\{J(t)\} = \frac{1}{\mu_0} + J_a\left(\frac{1}{p\tau}\right)^k \Gamma[k+1]$$

Fig. 16 Power-law (rheological) model for the description of deviatoric creep of bitumen/asphalt: model parameters, creep compliance function, and Laplace-Carson transform of creep compliance

Table 1. Composition of types of asphalt considered in experimental program

Asphalt type	Bitumen	Filler	Aggregate 0-4mm	Aggregate 4-22mm	Air
	[vol-%]	[vol-%]	[vol-%]	[vol-%]	[vol-%]
SMA11-B70/100-D	15.7	3.7	23.1	54.4	3.1
SMA11-PmB45/80-65-D	15.5	3.7	22.9	54.1	3.7

The viscous properties of asphalt are resulting exclusively from the time-dependent behavior of bitumen. These properties represent input for upscaling of viscoelastic properties within the multiscale model depicted in Fig. 15. The time-dependent behavior of bitumen is identified using two types of experiments, namely the Bending Beam Rheometer (BBR) and the Dynamic Shear Rheometer (DSR).

Based on these experiments, the creep compliance of bitumen was found to be approximated well by the Power-Law (PL) model, with the compliance function and the Laplace Carson transformation reading (see Fig. 16)

$$J(t) = \frac{1}{\mu_0} + J_a\left(\frac{t}{\tau}\right)^k \rightarrow J^*(p) = \frac{1}{\mu_0} + J_a\left(\frac{1}{p\tau}\right)^k \Gamma[k+1] \tag{19}$$

In Eq. (19), μ_0 [MPa] is the (elastic) shear modulus, J_a [MPa^{-1}] is the viscous part of the creep compliance at $t = \bar{\tau}$, and k is the creep exponent.

With the time-dependent properties of bitumen at hand, continuum micromechanics is employed to predict the viscous properties of asphalt. Two types of asphalt were considered:

- a split mastic asphalt with bitumen B70/100, and
- a split mastic asphalt with polymer modified bitumen PmB 45/80-65.

The so-obtained viscoelastic properties of asphalt were assessed by static asphalt creep tests conducted at different temperatures. Hereby, the load level was adapted to the tensile strength of asphalt at the respective testing temperature. For upscaling, the identified values of k and J_a for the considered type of bitumen served as input together with the mix design of the respective asphalt mixture (see Table 1) and the properties of the aggregates.

Figs. 17 and 18 show the viscous model parameters predicted by the multiscale model (four upscaling steps, using the Mori-Tanaka scheme) and the respective experimental data, highlighting the good performance of the presented mode of upscaling.

Finally, the presented mode of upscaling is employed for assessment of the performance of

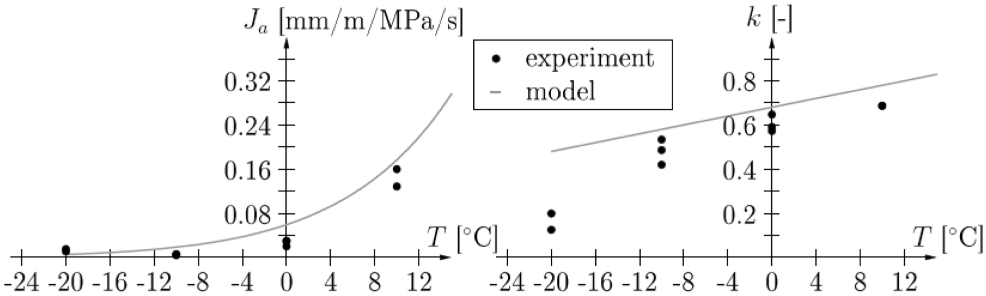

Fig. 17 Multiscale prediction and experimental validation using static creep tests for asphalt SMA11 with bitumen B70/100

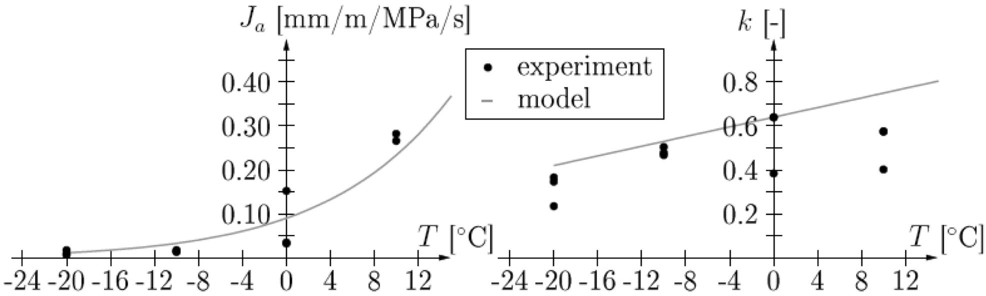

Fig. 18 Multiscale prediction and experimental validation using static creep tests for asphalt SMA11 with polymer modified bitumen PmB45/80-65

flexible pavements. For this purpose, a standard road section, consisting of a bituminous wearing course of stone-mastic asphalt SMA11, a base layer of high modulus asphalt concrete BT22, an unbound base course/sub-base of coarse gravel, and a sub-grade, are considered.

The lateral confinement of asphalt induces three-dimensional stress states. Therefore, the one-dimensional viscoelastic models are extended to three dimensions, introducing the (fourth-order) normalized compliance tensor $\underset{\sim}{G}$. Accordingly, the viscoelastic-strain tensor in consequence of three-dimensional loading, represented by the history of the stress tensor, is given by the convolution integral as

$$\underset{\sim}{\varepsilon}^{ve}(t) = \int_0^t J(t-\tau)\underset{\sim}{G}:\frac{\partial \underset{\sim}{\sigma}}{\partial \tau}d\tau \tag{20}$$

The cross section is subjected to a combination of thermal and traffic loading. The solution of the coupled thermo-mechanical problem is performed in two steps: First, the temperature distribution in the road section is determined on the basis of the prescribed temperature cooling scenario at the pavement surface by

$$\underset{\sim}{\sigma}_{n+1} = \underset{\sim}{C}:(\varepsilon_{n+1} - \varepsilon^{ve}_{n+1} - \varepsilon^{T}_{n+1}) \tag{21}$$

The so-obtained temperature profiles serve as input for the second step: mechanical analysis, considering thermal shrinkage, change of material parameters with temperature (provided by the

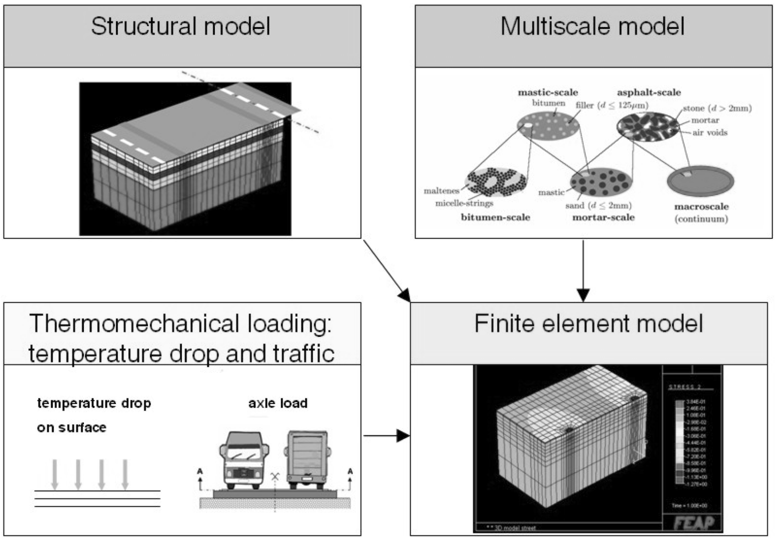

Fig. 19 Input for 3D finite element model for the analysis of flexible pavements

multiscale model) and, finally, the traffic load. Fig. 19 shows the input-scheme for the 3D finite element model for the analysis of flexible pavements used for performance-based optimization of flexible pavements.

5. Conclusions

Based on the results from this study, the writers are optimistic that multiscale analysis in civil engineering is a new technology that will survive because the construction industry will find “a good use” (Fish 2008).

References

Aigner, E. and Lackner, R. (2008), Micromechanics-based determination of viscous properties of asphalt concrete. *J. Mater. Civil Eng*. ASCE (accepted for publication).

Aigner, E., Lackner, R. and Pichler, C. H. (2007), “Bottom-up” Multiscale Modeling of Viscoelastic Properties of Asphalt. Proc. of the International Conference on Advanced Characterisation of Pavement and Soil Engineering Materials, (Eds.: A. Loizos, T. Scarpas, I. L. Al-Qadi), Taylor & Francis Group, ISBN: 978-0-41544882-6 123-135.

Dormieux, L., Molinari, A. and Kondo, D. (2002), “Micromechanical approach to the behavior of poroelastic materials”, *J. Mech. Phys. Solids*, **50**, 2203-2231.

Eshelby, J. D. (1957), “The determination of the elastic field of an ellipsoidal inclusion, and related problems”, *Proc. Royal Soc. London*, **A 241**, 376-396.

Fengel, K. and Wegener, G. (2003), Wood. Chemistry, Ultrastructure, Reactions. Verlag Kessel, Remangen.

Feret, R. (1892), “On the compactness of hydraulic mortars [Sur la compacitée des mortiers hydrauliques]”, *Annales des Ponts et Chaussées*, **4**(7), 5-161.

Fish, J. (2008), "Multiscale computations: boom or bust", *IACM Expressions* **22**, 4-7.

Fleischmann, M., Krenn, H., Eberhardsteiner, J. and Schickhofer, G. (2007), "Numerische Berechnung von Holzkonstruktionen unter Verwendung eines orthotropen elasto-plastischen Werkstoffmodells", *Holz Roh-Werkstoff*, **65**, 301-313.

Fritsch, A. and Hellmich, C. (2007), "'Universal' microstructural patterns in cortical and trabecular, extracellular and extravascular bone materials: micromechanics-based prediction of anisotropic elasticity", *J. Theor. Biol.*, **224**, 597-620.

Gould, S. J. and Lewontin, R. C. (1979), "The spandrels of San Marco and the Panglossian paradigm: a critique of the adaptionist programme", *Proc. Royal Soc. London*, **B 205/1161**, 581-598.

Hellmich, C. and Mang, H. (2005), "Shotcrete elasticity revisited in the framework of continuum micromechanics: From submicron to meter level", *J. Mater. Civil Eng.* ASCE, **17**, 246-256.

Hellmich, C., Ulm, F. J. and Mang, H. A. (1999), "Consistent linearization in finite element analysis of coupled chemo-thermal problems with exo- or endothermal reactions", *Comput Mech*, **24**, 238-244.

Hellmich, C., Mang, H. and Ulm, F. J. (2001), "Hybrid method for quantification of stress states in shotcrete tunnel shells: Combination of 3D in situ displacement measurements and thermochemoplastic material law", *Comput Struct*, **79**, 2103-2115.

Hellmich, C., Ulm, F. J. and Mang, H. A. (1999), "Multisurface chemoplasticity. I: Material model for shotcrete", *J. Eng. Mech. (ASCE)*, **125**(6), 692-701.

Hofstetter, K., Hellmich, C. and Eberhardsteiner, J. (2005), "Development and experimental verification of a continuum micromechanics model for the elasticity of wood", *Eur. J. Mech. A-Solids* **24**, 1030-1053.

Hofstetter, K., Hellmich, C. and Eberhardsteiner, J. (2007), "Micromechanical modeling of solid-type and plate-type deformation patterns within softwood materials. A review and an improved approach", *Holzforschung*, **61**, 343-351.

Lackner, R., Blab, R., Jäger, A., Spiegl, M., Kappl, K., Wistuba, M., Gagliano, B. and Eberhardsteiner, J. (2004), Multiscale modeling as the basis for reliable predictions of the behaviour of multi-composed materials. Progress in Engineering Computational Technology, (Eds.: B.H.V. Topping, C.A. Mota Soares), Chapter 8, Saxe-Coburg Publications 153-187.

Laws, N. (1977), "The determination of stress and strain concentrations at an ellipsoidal inclusion in an anisotropic material", *J. Elasticity*, **7**(1), 91-97.

Lechner, M., Hellmich, C. and Mang, H. A. (2001), Short-term creep of shotcrete-thermochemoplastic material modelling and nonlinear analysis of a laboratory test and of a NATM excavation by the Finite Element method. Lecture Notes in Physics-Continuous and discontinuous modelling of cohesive-frictional materials, P. Vermeer, S. Diebels, W. Ehlers, H. Herrmann, S. Luding, and E. Ramm (eds.), Vol 568, Springer, Berlin, 47-62.

Macht, J., Lackner, R., Hellmich, C. and Mang, H. A. (2001), Shotcrete creep properties-review of material tests and structural analyses of tunnels. Proceedings of the 6th International Conference on Creep, Shrinkage, and Durability Mechanics of Concrete and Other Quasi-Brittle Materials, F.J. Ulm, Z. Bažant, and F. Wittmann (eds.), Cambridge, Massachusetts, USA, Elsevier Science Ltd., Amsterdam, 285-300.

Mackenzie-Helnwein, P., Müllner, H. W., Eberhardsteiner, J. and Mang, H. A. (2005), "Analysis of lay-ered wooden shells using an orthotropic elasto-plastic model for multiaxial loading of clear spruce wood", *Comp. Meth. Appl. Mech. Eng.*, **194/21-24**, 2661-2685.

Mura, T. (1987), Micromechanics of Defects in Solids. 2nd edn, Martinus Hijhoff, Dordrecht.

Pichler, B., Hellmich, C. and Eberhardsteiner, J. (2009), "Spherical and acicular representation of hydrates in micromechanical model for cement paste - Prediction of early-age elasticity and strength", *Acta Mech.*, **203**(3-4), 137-162.

Pichler, B., Scheiner, S. and Hellmich, C. (2008), "From micron-sized needle-shaped hydrates to meter-sized shotcrete tunnel shells: Micromechanical upscaling of stiffness and strength of shotcrete", *Acta Geotechn.*, **3**(4), 273-294.

Scheiner, S., Pichler, B., Hellmich, C. and Mang, H. A. (2008), Damage and disaster prevention in NATM tunnels during construction: micromechanics-supported hybrid analysis. Proc. of the NATO Advanced Research Workshop on Damage Assessment and Reconstruction after Natural Disasters and Previous Military Activities (Eds. A. Ibrahimbegovic, M. Zlatar) Springer, 145-171.

Sercombe, J., Hellmich, C., Ulm, F. J. and Mang, H. A. (2000), "Modeling of early-age creep of shotcrete. I: Model and model parameters", *J. Eng. Mech. ASCE*, **126**, 284-291.

Stehfest, H. (1970), "Algorithm 368: Numerical inversion of Laplace transforms", *Commun ACM*, **13**, 47-49.

Stürzenbecher, R., Hofstetter, K., Bogensperger, T., Schickhofer, G. and Eberhardsteiner, J. (2008), "A continuum micromechanics approach to elasticity of strand-based engineered wood products: model development and experimental validation. Composites with micro- and nano-structure: Computational modeling and experiments (Ed. V. Kompis), Springer, 161-179.

Ulm, F. J. and Coussy, O. (1996), "Strength growth as chemo-plastic hardening in early-age concrete", *J. Eng. Mech*. ASCE, **122**(12), 1123-1132.

Zaoui, A. (2002), "Continuum micromechanics: Survey", *J. Eng. Mech*. ASCE, **128**, 808-816.